SUPPLEMENTAL INFORMATION FOR:

Subtypes of medulloblastoma have distinct developmental origins.

Paul Gibson, Yiai Tong, Giles Robinson, Margaret C. Thompson, D. Spencer Currle, Christopher Eden, Tanya A. Kranenburg, Twala Hogg, Helen Poppleton, Julie Martin, David Finkelstein, Stanley Pounds, Zoltan Patay, Matthew Scoggins, Robert Ogg, Yanxin Pei, Sonja Brun, Youngsoo Lee, Frederique Zindy, Janet C. Lindsey, David H. Gutmann, Frederick A. Boop, Robert A. Sanford, Amar Gajjar, Steven C. Clifford, Martine F. Roussel, Peter J. McKinnon, Makoto M. Taketo, David W. Ellison, Robert Wechsler-Reya, Richard J. Gilbertson.

Correspondence should be addressed to RJG: Richard.Gilbertson@stjude.org

CONTENTS

Supplemental Methods	**p3**
Supplemental Figure 1	**p18**
Supplemental Figure 2	**p19**
Supplemental Figure 3	**p20**
Supplemental Figure 4	**p21**
Supplemental Figure 5	**p22**
Supplemental Figure 6	**p24**
Supplemental Figure 7	**p25**
Supplemental Figure 8	**p26**
Supplemental Figure 9	**p28**
Supplemental Figure 10	**p29**
Supplemental Figure 11	**p30**
Supplemental Figure 12	**p31**
Supplemental Figure 13	**p32**
Supplemental Figure 14	**p33**

Supplemental Methods

Human studies

Patient samples and Magnetic Resonance imaging (MRI). Tumor samples were obtained with appropriate informed consent and Institutional Review Board approval from patients treated at St Jude Children's Research Hospital. Histological diagnosis was confirmed by central review (D.W.E.). RNA and DNA were isolated from tumor samples for microarray, reverse transcriptase Real-Time polymerase chain reaction (rtRT-PCR) and sequence analysis as described below.

Tumor imaging included T1-weighted scans before and after administration of a gadolinium-based contrast agent. The slice thickness was 5 mm and the in-plane resolution was 0.8mm. Pre- and post-operative T1-weighted images from all patients were spatially normalized[30], to the standard brain space defined by the Montreal Neurological Institute (MNI) brain template[31]. Spatial normalization was performed with Statistical Parametric Mapping software (SPM5, Wellcome Institute of Neurology, London, UK) using default parameters, except that the brain bounding box was extended from 50 to 80mm in the negative z-direction for sagittal images and all output images were resliced to 1mm x 1mm x 1mm resolution.

To characterize the accuracy of spatial normalization we defined a set of landmarks from the MNI space that were identified in the normalized images from each patient. The landmarks and their MNI coordinates (x, y, z) included the center of the anterior commissure (0, 5, -4), the cerebral aqueduct (0, -30, -10), a point on the posterior aspect of the brain stem in the fourth

ventricle (0, -34, -26), the apex of the cerebellum in the midline (0, -54, 4), lateral extremes of the cerebellum on the right (59, -58, -39) and left (-59, -58, -39), and inferior extremes of the cerebellum on the right (36, -56, -60) and left (-36, -56, -60)[32]. The locations of landmarks in the normalized images of each patient were measured with 3D Slicer software (version 3.4, www.slicer.org). The location of the tumor or the surgical cavity following resection was characterized in two ways. First, the coordinates of the visually apparent center of the tumor or surgical cavity were measured with 3D Slicer software. The distance of the center of the tumor or surgical cavity from the landmark at the posterior aspect of the brainstem and the angle from the midline to the tumor center (or center of the surgical cavity) in the xy-plane were calculated. Second, the cross-section of the tumor and surgical cavity at the location of the maximum apparent size was drawn for each patient in the transverse and sagittal planes. The cross-sections were rendered as color overlays on reference images to demonstrate the distribution of tumor location for the patients in each group. All image analysis was performed masked to tumor subtype.

Human medulloblastoma rtRT-PCR and sequencing. Total mRNA was isolated from the medulloblastomas described above. All tumor samples were obtained prior to administration of any chemo- or radiotherapy. Total RNA was extracted from tumors using Trizol (Invitrogen) according to the manufacturer's instructions. 1μg RNA from each tumor was reverse transcribed to produce cDNA. For rtRT-PCR, cDNA was amplified by Taq polymerase, using primers specific for WIF1, DKK1, GAD1, ATOH1, GLI1 and SFRP1 as described previously (reference 3 main paper). Production of double-stranded DNA was quantified using SYBR Green (BioRad) and MyiQ detection software (BioRad). Data for each gene were normalized to the reference

gene, r18S. Real-Time PCR was also used as described previously (see Reference 3 in main manuscript) to validate regions of deletion on chromosome 6 as reported in Figure 4c of the main manuscript. Primer and probe sets used to validated inferred homozygous deletion on chromosome 6 were:

(1) SEC5L1. 6p25.3:

forward CGTACAGCAGAATCTTTCAGGCTTA

reverse TTGGAGAAATGGCTGATGCA

probe TTGTCCTTGCCCTGCCTCAGCC.

(2) BMP6. 6p24.3:

forward CCCATCCGCCACACAAA

reverse GGATGCCAAGAGAAAGCTGAA

probe CATGAGCTGTTACACATCCCGAGTAATGAAGTG.

(3) TXNDC5 6p24.3:

forward TGGCTTCTGCAGGGTTATCC

reverse TTTGCCAACATCAGGTCACAACTT

probe GTGACTCACAAACTGGCCATACA.

(4) HIST1H2. 6p21.2:

forward CAACCTCAACCTAAGTAATTTCTCATCTT

reverse ATAACTGCCTGGTGCTTTGCA

probe CCAGGGTCTTGCATTTTGTGGATGCTTAAT.

(5) DNAH8. 6p21.2:

forward TGCAGCTGTCACTTGGAATAGC.

reverse AACAAGCTGGTAGCATGTTAATTAGTTC.

probe TTTCCCTACTGTGCATATTATGCC

(6) MDGA1. 6p21.2:

forward GGATTGGAAGCTGTGTAGAAAAGTG.

reverse TGAAAAAGCTCTCCAGGTGGTT.

probe TTCTCAGCCCTGGCGCATGTCA

(7) KCNK5. 6p21.2:

forward CCACCATTGGATATGGCAATG.

reverse CGAAGAGACCATAGAAAACACAGAAG.

probe CCCAAGACCCCCGCCGGT.

(8) COL9A1. 6q13:

forward TCTTCTTGATCGGTGACTTAGGTACTAA.

reverse TGCCTCATGCGAATACAAGTG.

probe TCACTTTTTCTCTCTGTTCTCGCTATTCTCTCTCATCT.

(9) LAMA4. 6q21:

forward TCTCCTTTGGTGGTCTCCTTTAAT.

reverse TGTTCAGAAAAGAGACCTCAATGG.

probe TAAAGTTTGTTTTGCTGCACTCTGAGCTATGTTACAG.

(10) MARCKS. 6q21:

forward CCCCTCTTGGATCTGTTGAGTT.

reverse CGCTGCGGTCTTGGAGAA.

probe TTGAAGAAGCCAGCATGGGTGCC.

(11) FRK1. 6q21:

forward TGCTGAATGAAGAGGAGCTGAA.

reverse TGGTGCCACCAGGAAAAAG.

probe TCTGAGCCCCCAGGACTGACATTTCA.

(12) LAMA2. 6q22.33:

forward ATTTGACCCATCAGACCTTTGAG.

reverse TGGTGAGTGTTGTAATTATGTTCCATT.

probe CACGTGCAGGAAGCCAAGTTTAAGGAAA.

(13) AK097143. 6q24.1:

forward GCCAAATTTTACTCCCATCTCTTC.

reverse TGTTATATCCTCACCTTCCAGTTCCT.

probe CCTAATGGATTCCTTTGCTTTGCTTACTCAGGTC.

(14) ZDHHC14. 6q25.3:

forward AGCACACTGCTTTGCGTATAGTG.

reverse TTTACAAAGTCTCAAATTCATCTCCTTTC.

probe TGATTGATTGGGCTAGGTTAGTGTTGCTGG.

Exon three of *CTNNB1* was sequenced in each tumor sample as described (reference 3 main paper). *TP53* was sequenced in tumor and peripheral blood samples using established primers and protocols[33].

Mouse studies

Developmental gene expression mapping using Brain Explorer 2. Using Affymetrix U133 v 2 expression microarrays we previously identified the top 110 genes that are most significantly and differentially expressed between human SHH and WNT-subtype medulloblastomas (see

Reference 3 in the main text and Supplemental Dataset 1 and Supplemental Table 1). *In situ* hybridization data reporting the expression of 49 of these genes (24 of WNT-subtype and 25 of SHH-subtype medulloblastoma) were available within Brain Explorer 2 (www.brain-map.org) produced by the Allen Institute for Brain Science. Brain Explorer 2 is a desktop software application for viewing the Allen Developing Mouse Brain Atlas gene expression data in the framework of the Allen Developing Mouse Brain Reference Atlas. Brain Explorer 2 supports full interactive viewing of gene expression in the Allen Developing Mouse Brain Reference Atlas in 3-dimensions throughout the entire thickness of the brain at 7 developmental ages. These 3-D images are presented at a resolution of 80μm and can be co-registered to, and visualized within, the context of specific developmental landmarks e.g., rhombomeres. Furthermore, multiple images of different genes from the same age can be superimposed on one another in 3-D. One particularly powerful function within Brain Explorer 2 is the linking of all pixels in 3-D expression maps to the original *in situ* hybridization stained sections. This link allows investigators to view the precise original staining data that was used to generate 3-D expression distributions.

Full descriptions of the staining procedures and 3-D anatomical modeling algorithms used to generate the expression data within Brain Explorer 2 are provided at http://developingmouse.brain-map.org/content/explorer. Briefly, we accessed the original *in situ* hybridization data at E11.5, E13.5 and E15.5 for all 24 WNT-subtype and 25 SHH-subtype medulloblastoma signature genes within Brain Explorer 2. Focusing on the hindbrain, the expression data for each of these genes was reviewed in detail and reported in three separate

results pages for each gene within Supplemental Dataset 1. **Page 1** for each gene displays high-resolution images of *in situ* stained sections downloaded from www.brain-map.org that report the most representative expression patterns for that gene. Brain Explorer 2 was then used to generate 3-D expression maps for each gene across rhombomeres 1-8 in both sagittal and coronal planes. These maps were built for developmental stages E11.5 (reported on **page 2**) and E15.5 (reported on **page 3**) for each gene within Supplemental Dataset 1. Finally, for each set of signature genes, we generated regional gene expression maps (at E11.5 and E15.5) by overlaying in Brain Explorer 2 the 3-D data for each gene and plotting the common regions of overlap and the percentage of subgroup signature genes expressed within each region of overlap. These data are reported in Figures 1a and b of the main manuscript.

Developmental gene expression mapping using additional online databases. Gene expression data images were also available at ~E15.5 for an additional 22 human WNT-subtype and 39 SHH-subtype medulloblastoma signature genes from the BGEM database (www.stjudebgem.org), Gene paint (www.genepaint.org) and the GENSAT database (www.gensat.org). Similar to the Allen Brain Atlas, Gene paint datasets employ non-radioactive histochemical staining to visualize probe hybridization, therefore preserving histological detail. In contrast to the other datasets GENSAT reports immunohistochemical stains of enhanced green fluorescence protein (EGFP) in BAC transgenic mice in which the appropriate endogenous protein coding sequences have been replaced by sequences encoding the EGFP reporter gene.

We performed a manual review of all sections for each of the 22 human WNT-subtype and 39 SHH-subtype medulloblastoma signature genes in each data set. We observed remarkable

agreement in the expression data reported for each gene by these three independent online resources. For each gene we noted if the gene of interest was expressed in either the EGL, VZ and/or LRL. Importantly, the GENSAT and Genepaint databases allow for high-resolution 'zooming' of images that allow detailed high-magnification review of sections on which the EGL, VZ and LRL are readily identified. These data are recorded in Supplemental Table 1.

Genetically engineered mice. All experimental methods, including surgical procedures, were performed according to approved ACUC protocols. The generation of *Blbp-Cre*, *Ctnnb1*$^{lox(ex3)}$, and *Tp53*^{flx} mice have been described previously (see reference 17,18,20 in main paper). *Rosa-YFP* reporter mice were obtained from the Jackson Laboratories. To create *Atoh1-Ctnnb1*$^{\Delta N90}$ mice we cloned a 1.7kb fragment of the *Atoh1* enhancer region (generous gift of Jane Johnson)[34] upstream of a truncated and constitutively active Ctnnb1-green fluorescence fusion protein (reference 22 main paper). Three independent transgenic lines were generated by pronuclear injection of the *Atoh1-Ctnnb1*$^{\Delta N90}$ construct into FVB zygotes. Each line transmitted the expressing transgene in the germline. For tumorigenesis studies, of *Atoh1-Ctnnb1*$^{\Delta N90}$ and all other mice, $\geq$50 mice of appropriate genotype (or littermate controls) were observed daily for signs of neurological impairment or evidence of non-neurological pathology. Mice were then euthanized and the brains removed and processed appropriately.

In utero **electroporation and cell tracking (see Supplemental Figures 10-11).** Pregnant mice bearing E12.5 embryos were deeply anaesthetized and the uterus externalized under sterile conditions. A drawn-glass needle was then inserted through uterine wall into the fourth ventricle of each embryo. 1µL of a 1µg/µL solution of *CMV-eGFP* plasmid DNA containing 0.01% Fast

Green (Sigma) for enhanced visualization was injected into the ventricle. Electroporation of plasmid DNA into the embryonic precerebellar neuroepithelium (PCN) was performed using a CUY-21 electroporator (Nepa Gene Co. Ltd., Tokyo, Japan) with a potential difference of 50V for 50ms, followed by a rest period of 950ms. The electrodes were placed on the exterior of the uterus, across the embryonic head such that DNA was drawn down into the brainstem. This was repeated 5 times for each embryo whose positioning within the uterus allowed access to the hindbrain. The uterus was then replaced inside the female, and the wound sutured. Females delivered normally and on the day of birth, pups were anesthetized on ice, then transcardially perfused with 4% w/v paraformaldehyde in phosphate buffered saline (PBS). Brains were dissected from the pups. The transduced brain was then placed beneath a fluorescence-enabled microscope and images were captured using Elements software (Nikon). Fluorescence ratios in the PCN:pontine nuclei were measured using ImageJ software (National Institutes of Health, USA). The brains were then cryopreserved and embedded and eGFP expression localized in sections by direct visualization of fluorescence in 12μm sections counterstained with DAPI.

Granule Neuron Precursor Cell (GNPC) cultures. GFP^+ GNPCs were isolated by FACS from the cerebella of P7 *Atoh1*-GFP transgenic mice. GNPCs were cultured in poly-D-lysine-coated 96-well plates at 2×10^5 cells per well. Mutant-*Ctnnb1*-GFP or control GFP virus, Wnt1 protein (50ng/ml) (PeproTechInc Catlog#: 120-17), or Shh supernatant (3ug/ml) were added and incubated for 48 hours before being pulsed with [*methyl*-3H]thymidine (GE Healthcare, Piscataway, NJ). After 16 hours, cells were harvested by using a Mach IIIM Manual Harvester 96 (TOMTEC, Hamden, CT), and incorporated radioactivity was quantitated using a Wallac MicroBeta microplate scintillation counter (PerkinElmer, Fremont, CA).

Microdisection of the embryonic LRL. Embryonic E16.5 *Blbp-Cre* ; *Ctnnb1*$^{lox(ex3)}$; *Tp53*$^{fxl/flx}$ and *Ctnnb1*$^{lox(ex3)}$; *Tp53*$^{fxl/flx}$ mice were obtained from deeply euthanized pregnant females. The hindbrain of each embryo was exposed by dorsal incision and the cerebellum carefully removed by microscope assisted dissection to reveal the floor of the IVth ventricle. The LRL lateral to the floor plate was then gently pared away from the brainstem by microdissection and snap frozen over liquid nitrogen. Several LRL isolates were 'pooled' together from embryos of the same genotype to obtain adequate mRNA for gene expression profiling as described below.

Bromodeoxyuridine (BrdU) labeling and chasing. Pregnant mice carrying E12.5 *Blbp-Cre* ; *Ctnnb1*$^{lox(ex3)}$; *Tp53*$^{flx/flx}$ and *Ctnnb1*$^{lox(ex3)}$; *Tp53* $^{flx/flx}$ embryos were injected intraperitoneally with 50mg/kg bodyweight BrdU (Sigma) in PBS. 24 hours later, embryos were harvested and fixed with 4% paraformaldehyde for 24 hours at 4^{o}C. Following embedding in paraffin, 5µm sections were then analyzed by dual immunofluorescence using antibodies specific for BrdU (Sigma; mouse; 1:500) and Ki67 (Vector Labs; rabbit; 1:1000) and fluorescently-labeled secondary antibodies (BrdU detected using AlexaFluor 594-conjugated goat anti-mouse antibody; Ki67 detected using AlexaFluor 488-conjugated goat anti-rabbit antibody). The percentage of BrdU^{+}/Ki67^{-} and BrdU^{+}/Ki67^{+} cells was identified within the sPCN of five sections of each embryo randomly chosen sections.

Histology

Tissue staining. Brains were post-fixed in 4% paraformaldehyde (PFA) for 24 hours and then processed through a graded series of ethanols into xylene and then paraffin wax. Wax-embedded

tissues were sectioned at 5μm thicknesses and mounted on SuperfrostPlus microscope slides (Fisher Scientific). Hematoxylin/eosin (H&E; Fisher Scientific) stains of de-waxed and rehydrated sections were performed to a standard protocol. Standard immunohistochemical methods were to detect proteins in tissue sections using the following antibodies: mouse anti-β catenin (Becton Dickinson, 610154, 1:250); rabbit anti-Ki67 (VectorLabs, VP-RM04, 1:1000); rabbit anti-Pax6 (Covance, PRB-278P, 1:400). For immunofluorescence, a standard protocol was used to in association with anti-β catenin (Becton Dickinson, 610154, 1:250), Rabbit anti-Zic1 (Rockland), rabbit anti-Olig3 (generous gift of Carmen Birchmeier), anti-Ptf1a (generous gift of Jane Johnson) and two different anti-GFP antibodies (chicken, Abcam Inc., and rabbit, Invitrogen Corp). Nuclei were counterstained with 4',6-diamidino-2-phenylindole (DAPI; Vector Labs). Cells undergoing apoptosis were detected with the Apoptag kit (Millipore, S7100), in accordance with the manufacturer's instructions. Sections were lightly counterstained with hematoxylin.

β-galactosidase staining. Whole brains were post-fixed in 2% PFA overnight at 4^{o}C, then cry-protected by immersion in 30% sucrose overnight at 4^{o}C. Brains were cut sagitally and embedded in OCT over dry ice. Sections were cut at 12μm, OCT removed by washing with PBS, and then incubated with a β-galactosidase substrate solution (1mg/ml X-gal; 5mM potassium ferricyanide; 5mM potassium ferrocyanide; 2mM MgCl2; 0.01% sodium deoxycholate; 0.02% NP-40 in PBS) overnight at 37^{o}C. Sections were washed extensively in water, then counterstained with Fast Red.

Volumetric measurements of the LRL. Paraffin-embedded mouse brains were sectioned at 5μm, sagitally, across the entire width of the brain. Twenty to thirty sections per brain spaced every 100μm were H&E stained. Each section was examined at 10X magnification, and the area occupied by the LRL was outlined manually within BioQuant Nova Prime software (Bioquant Image Analysis Corp.). Two-dimensional outlines of sections were arranged in three-dimensional space (distance between sections constituting the z-axis) to calculate LRL volumes.

mRNA and DNA microarray analysis

mRNA expression profile analysis. Human mRNA gene expression profiles of WNT and SHH-subtype medulloblastomas were generated previously (reference 3 main paper). mRNA expression profiles were generated from mouse tumors and tissues using 430v2 microarrays (Affymetrix, Santa Clara, CA). Gene expression data were normalized using the MAS 5.0 algorithm. The data were then transformed and variance stabilized by addition of a small factor of 20 that shrinks the effects of small numbers and then taking the natural logarithm. The data were then imported into Spotfire Decision Site (Palo Alto CA, USA) and for each probe set and sample z-scores were calculated by computing the mean and standard deviation across samples within each probeset.

Ortholog selection. Matching of mouse 430v2.0 probesets with human Affymetrix probesets was made possible through an ortholog mapping file provided by Affymetrix. Nearly all of the probesets that had orthologs represented on microarrays of both species were reference sequences. Redundant probes were removed (based on MAD) so that no mouse probeset or

human probeset appeared more than once. 11,049 common orthologs were identified for the human and mouse Affymetrix datasets.

Agreement of differential expression (AGDEX). For a detailed description of the AGDEX algorithm please see Ref. 13 in the main manuscript. The agreement of differential expression between transcriptomes observed in human and mouse tissues was evaluated using a novel statistical procedure developed for the current study that we have called agreement of differential expression (AGDEX). Differential expression between two distinct groups of human samples (Medulloblastoma-subtypes were defined in Thompson et al., (Reference 3 of the main manuscript) was defined by the difference of the mean log-transformed expression values for each gene. Similarly, the differential expression between two groups of mouse samples (*Blbp-Cre*$^{+/-}$; *Ctnnb1*$^{+/lox(ex3)}$; *Tp53*$^{flx/flx}$ and *Ptch1*$^{+/-}$; *Tp53*$^{-/-}$ mouse medulloblastomas) was defined by the difference of mean log-transformed expression values for each gene. These differential expression results for each species were represented as a vector in multi-dimensional space. The statistical significance of the AGDEX statistic was determined via comparison to a null distribution for the agreement statistic obtained via 10,000 random permutations of the assignment of group labels for the human expression data. A new value of the agreement statistic was computed using the differential expression result for each permutation of the human data. In this manner, an empirical distribution for the agreement statistic under the null hypothesis of exchangeability of the human group labels was obtained. The p-value was defined as the proportion of permutations yielding an agreement statistic with greater absolute value than that of the observed agreement statistic.

DNA microarray analysis. Mouse genome-wide DNA microarray analysis was performed using the G4415A, Agilent Mouse CGH 244K array, consisting of 60mer in situ synthesized oligonucleotides (Agilent Technologies, Santa Clara, CA). This array contains 235,402 probes spaced across the mouse genome. Array hybridization was performed according to the manufacturer's recommended protocols. In brief, genomic DNA isolated from the indicated mouse tissues was labeled using the Agilent ULS Labeling kit. Hybridization was carried out in an Agilent oven at 65°C for 40 hours at 20 rpm, followed by standard wash procedures. The microarray was then scanned in an Agilent scanner at 3μm resolution, and the array data was extracted using the default CGH settings with Lowess dye bias correction normalization of Agilent Feature Extraction Software (v10.5.1.1). The circular binary segmentation algorithm implemented in the DNAcopy package from Bioconductor was then applied to the normalized log2 ratio data to identify copy number alterations for each sample. Copy number changes were characterized as probe segment value referred to as its "smoothed" value. The gain and loss status for each segment was assigned using threshold of one copy difference on consecutive probes across the genome. Data was further analyzed and visualized with Spotfire (TIBCO, Somerville, MA) and IGV (http://www.broad.mit.edu/igv).

Construction of Single Nucleotide Polymorphism (SNP) microarray profiles of human tumors. SNP microarray profiles were generated in collaboration with the Hartwell Center for Bioinformatics and Biotechnology at St Jude Children's Research Hospital using the Affymetrix GeneChip Human Mapping 500K assay which interrogates ~500,000 total SNPs with median inter-marker distance of 2.5kb. Purity and integrity of DNA samples was confirmed by UV spectrophotometry and by agarose gel electrophoresis. Processing of DNA samples was

performed according to the Affymetrix 500K SNP protocol. Briefly, total genomic DNA (250 ng) was digested to completion using NspI or StyI restriction enzyme and ligated to oligonucleotide adapters. Ninety micrograms of amplified DNA were fragmented using DNase I and end-labeled with biotinylated-nucleotide using terminal deoxynucleotidyl transferase. Labeled DNA targets were added to a hybridization cocktail containing array controls, blocking agents (human Cot-1 and herring sperm DNA), and incubated overnight at 48^{o}C on a GeneChip array. Arrays were washed and stained with Streptavidin Phycoerythrin (SAPE, Molecular Probes) using the GeneChip Fluidics Station 400, then scanned using an Affymetrix GeneChip Scanner 3000. SNP microarray data were analyzed using the general strategy of Mullighan et al.,[35]. Initial signal values were obtained using the Affymetrix PLIER algorithm. Genotype calls were generated using the BRLMM algorithm[36]. Subsequent signal processing and copy number analysis was performed separately for each tumor sample as described[35].

References

30 Ashburner, J. & Friston, K. J. Nonlinear spatial normalization using basis functions. *Hum Brain Mapp* **7**, 254-266 (1999).

31 Brett, M., Johnsrude, I. S. & Owen, A. M. The problem of functional localization in the human brain. *Nat Rev Neurosci* **3**, 243-249 (2002).

32 Schmahmann, J. D. *et al.* Three-dimensional MRI atlas of the human cerebellum in proportional stereotaxic space. *Neuroimage* **10**, 233-260 (1999).

33 Frank, A. J. *et al.* The TP53-ARF tumor suppressor pathway is frequently disrupted in large/cell anaplastic medulloblastoma. *Brain Res Mol Brain Res* **121**, 137-140. (2004).

34 Lumpkin, E. A. *et al.* Math1-driven GFP expression in the developing nervous system of transgenic mice. *Gene Expr Patterns* **3**, 389-395 (2003).

35 Mullighan, C. G. *et al.* Genome-wide analysis of genetic alterations in acute lymphoblastic leukaemia. *Nature* **446**, 758-764 (2007).

36 Carvalho, B., Bengtsson, H., Speed, T. P. & Irizarry, R. A. Exploration, normalization, and genotype calls of high-density oligonucleotide SNP array data. *Biostatistics* **8**, 485-499 (2007).

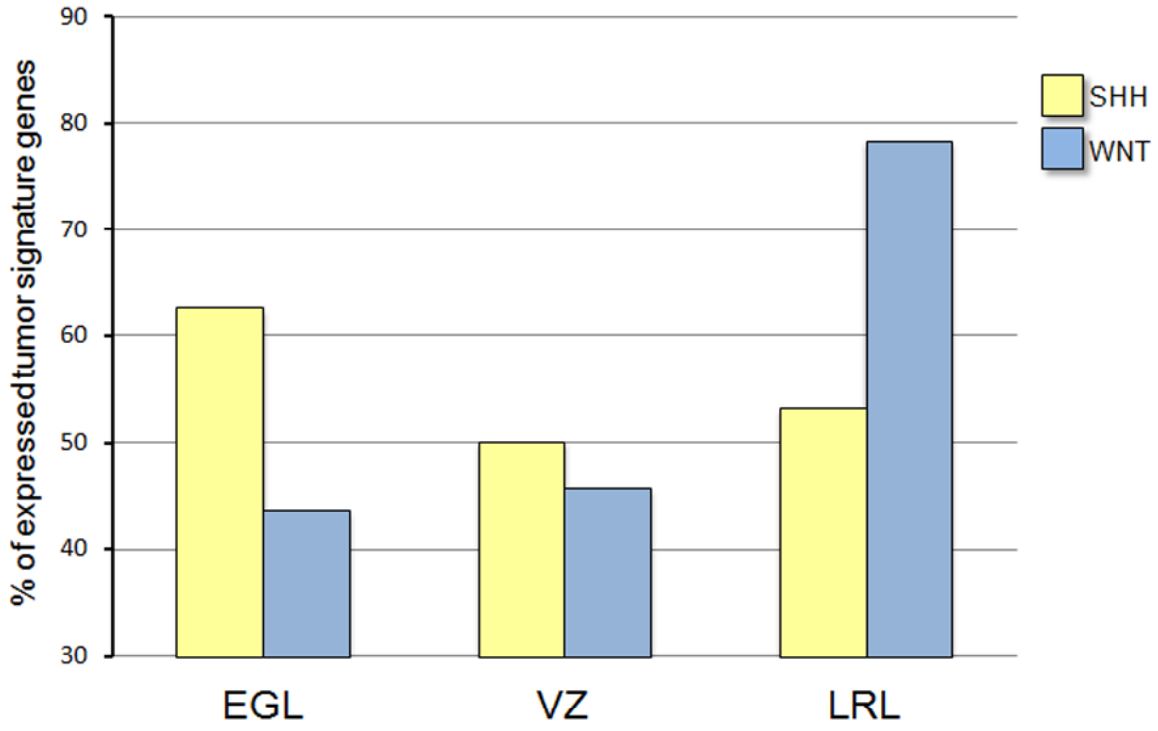

Supplemental Figure 1. Analysis of the distribution of expression in the embryonic (E14.5) mouse hindbrain of orthologs of key signature genes of human SHH and WNT-subtype medulloblastoma. Graph reports the percentage of 64 and 46 signature genes of human SHH and WNT medulloblastoma subgroups, respectively, that are expressed in the external germinal layer (EGL), ventricular zone (VZ) and lower rhombic lip (LRL) of the E14.5 mouse hindbrain. Data was derived from manual review of images archived within four publically accessible mouse gene expression databases (see Supplemental Methods). The expression distribution for each gene is reported in Supplemental Table 1. The detailed anatomical distribution of 24 and 25 of these human WNT-subgroup and SHH-subgroup medulloblastoma signature genes, respectively, is reported in Supplemental Dataset 1. Note the difference in anatomical expression distribution of the human SHH and WNT-subtype signature genes was significant (Chi-square $P<0.05$).

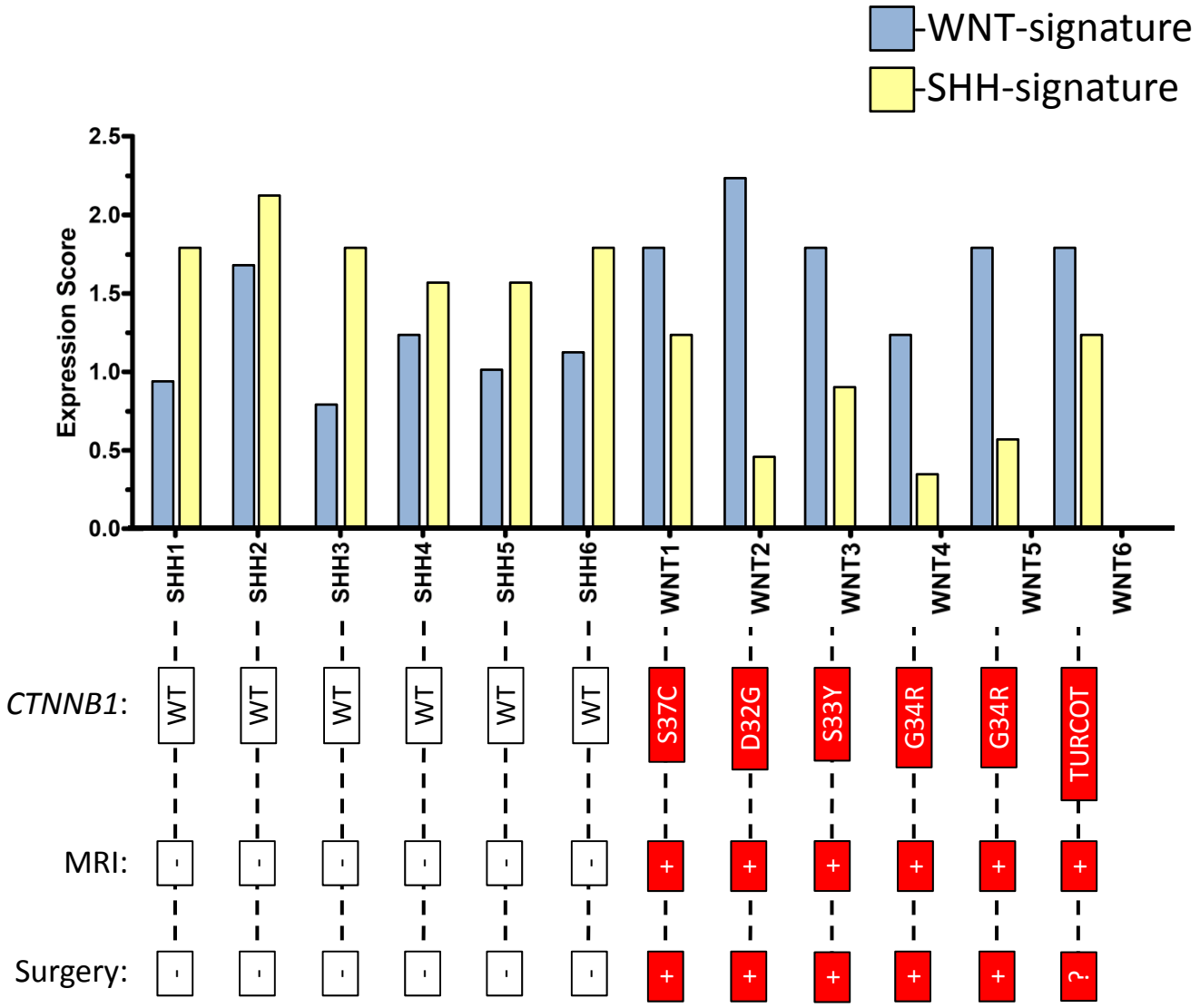

Supplemental Figure 2. Validation of WNT and SHH-subtype medulloblastomas used for MRI analysis. Graph at the top reports the composite reverse transcriptase Real Time-PCR score for key signature genes of WNT-subtype (*DKK1, GAD1, WIF1*) and SHH-subtype (*ATOH1, SFRP1, GLI1*) human medulloblastoma. Results for six SHH (1-6) and six WNT (1-6) are shown. Validation of this score as highly predictive of the corresponding subtype has been published previously (see Ref. 3 in primary manuscript and Supplemental Methods). Top boxes below report sequence changes in *CTNNB1* in the tumors (note WNT tumor 6 arose in a patient with Turcot's Syndrome). Middle boxes report evidence of brainstem infiltration on pre-operative MRI. Bottom boxes report evidence of brainstem infiltration at surgery. + =present, - =no evidence, ?=no specific comment in clinical notes.

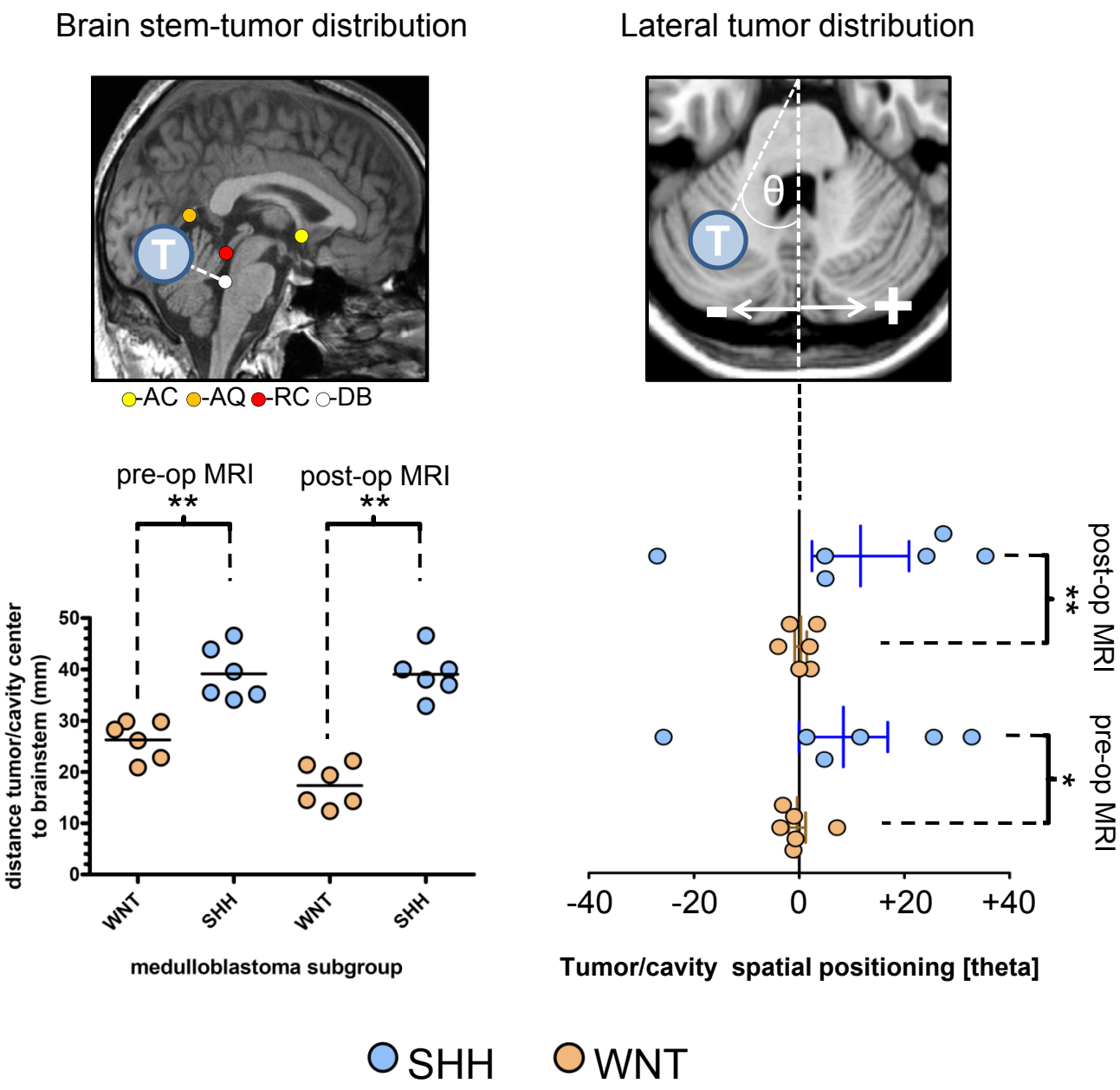

Supplemental Figure 3. Positional measurement in 3-dimensions within the hindbrain of WNT and SHH-subtype medulloblastomas. Image and graph to the left report brainstem-tumor distribution. Top left sagittal image shows the common anatomical points (anterior commissure, AC; aqueduct, AQ; rostral cerebellar boarder, RC; dorsal brainstem, DB) used to co-register all patient tumors in 3-D. The brainstem-tumor distance was measured in each case from the normalized DB to the center of the tumor (stylized example circled 'T' in cartoon). The lower left graph reports the pre and post-operative (tumor and cavity, respectively), brainstem-tumor distances for each of the six WNT and SHH-subtype tumors studied. Image and graph to the right report the position relative to the midline of each tumor. Top right axial image shows the angle of deviation from the midline (theta) calculated for each tumor. The lower right graph reports the pre and post-operative (tumor and cavity, respectively), theta for each of the six WNT and SHH-subtype tumors studied. Exact Mann-Whitney P values are *, <0.05 and **, <0.005 or ns, not significant. See Supplemental Methods for more details.

.

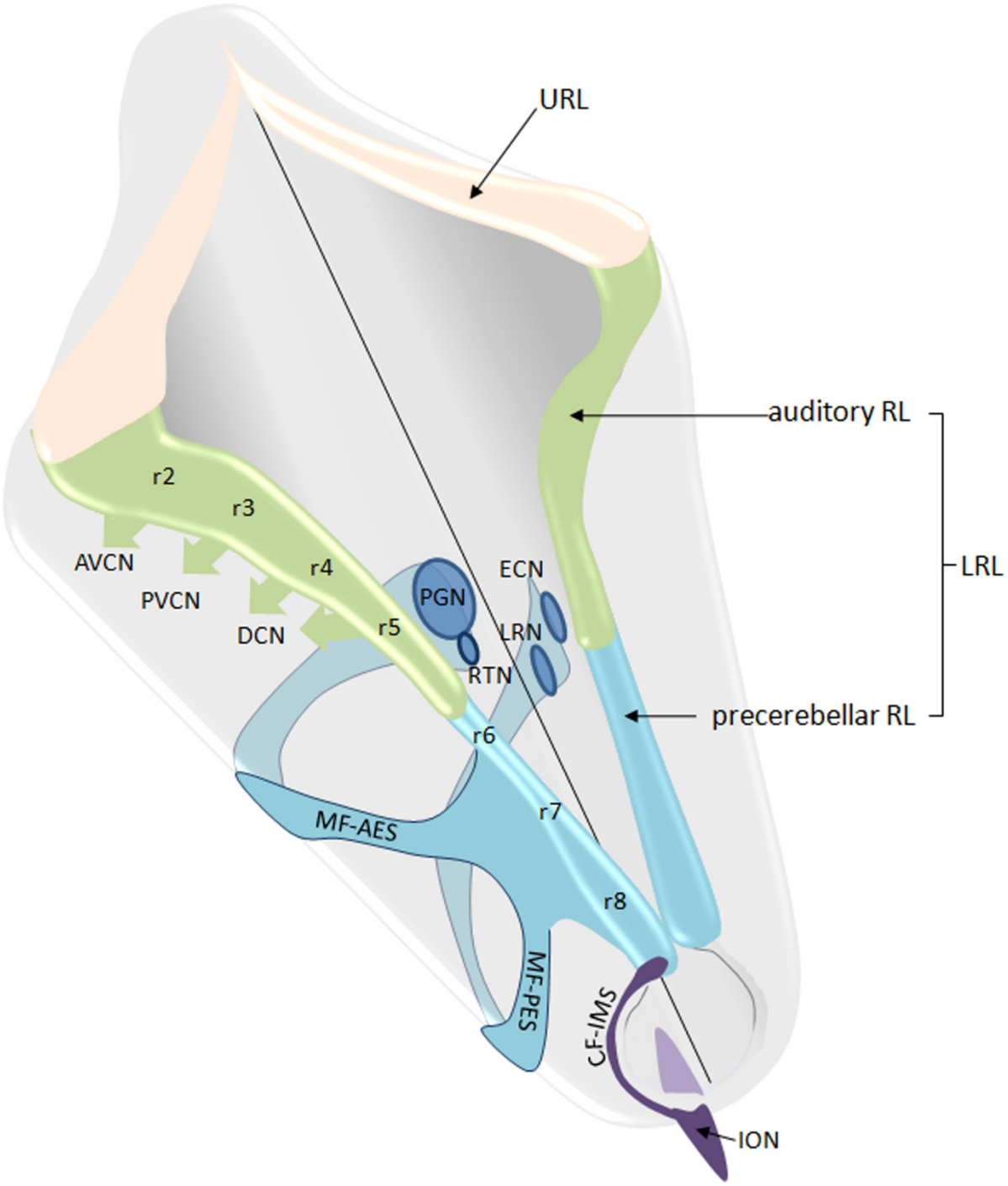

Supplemental Figure 4. Cartoon illustrating the fate of the two major divisions of the lower rhombic lip (LRL) during development (adapted from Ref. 15 and 25 in the main manuscript). The upper rhombic lip (URL, pink) comprising rhombomere (r) 1 generates the cerebellum. The lower RL can be divided into two major parts according the nuclei that each generates. The auditory RL (green) comprises r2–r5, and generates the anteroventral cochlear nucleus (AVCN), the posteroventral cochlear nucleus (PVCN), and the dorsal cochlear nucleus (DCN). The cochlear nuclei also receive contributions from the ventricular zone. The precerebellar RL (blue) comprises r6–r8. This region generates the mossy fiber (MF) streams (also in blue) that include the anterior extramural stream (AES), which gives rise to the Pontine Grey Nucleus (PN) and Reticular Tegmental Nucleus (RTN); and the posterior extramural stream (PES), which gives rise to the External Cuneate (ECN) and Lateral Reticulate Nucleus (LRN). The precerebellar RL also generates the intramural migratory stream (IMS, purple), that gives rise to the inferior olive nuclei (ION).

Supplemental Figure 5 (over leaf). Early and late developmental stage lineage tracing of Cre$^+$ cell progeny in the hindbrain of *Blbp-Cre* mice. (a) Sagittal and coronal **(b)** views of the hindbrain of embryonic day (E) 14.5 *Blbp-Cre*$^{+/-}$; *Rosa26*^{YFP} mice. Note the presence of the recombined YFP$^+$ allele in the three germinal zones of the hindbrain including the upper rhombic lip (URL)/external germinal layer (EGL); ventricular zone (VZ); and lower rhombic lip (LRL) (note the choroid plexus (cp) and other tissues are YFP$^-$, Scale bar=180µm). Regional high power views of the coronal section in (b) illustrating YFP labeling of cells in the LRL **(c)**, VZ **(d)** , URL **(e)**, EGL **(f)** (scale bars=50µm). Dual immunoflourescence of E14.5 *Blbp-Cre*$^{+/-}$; *Rosa26*^{YFP} mouse hindbrain confirming efficient *Blbp-Cre* induced recombination of the *RosaYFP* reporter allele among **(g)** Pax6$^+$ progenitor cells within the EGL; **(h)** Olig3$^+$ cells of the LRL (note the URL and choroid are Olig3$^-$); **(i)** Zic1$^+$ neurons of pontine grey nucleus (PGN). (Scale bar=50µm). **(j)** Left, low power sagittal view of a β-galactosidase stained hindbrain from an adult *Blbp-Cre*$^{+/-}$; *Rosa26*^{LacZ} mouse (Scale bar=800µm). Right, high power views of the internal granule cell layer (IGL), molecular layer (ML) and white matter (WM) in the cerebellum. The lower panel shows cells in the pontine grey nucleus (PGN) that are derived from the LRL. Scale bar=50µm. **(k)** DNA products generated by polymerase chain reactions (PCR) specific for the wild-type (WT) endogenous *Ctnnb1* allele (900p) and mutant (Mut) Cre-recombined *Ctnnb1*$^{lox(ex3)}$ allele (700bp) from DNA isolated from the indicated structures. The recombined allele was also detected in a medulloblastoma (medullo) that developed in a *Blbp-Cre* ; *Ctnnb1*$^{+/lox(ex3)}$; *Tp53*$^{flx/flx}$ mouse.

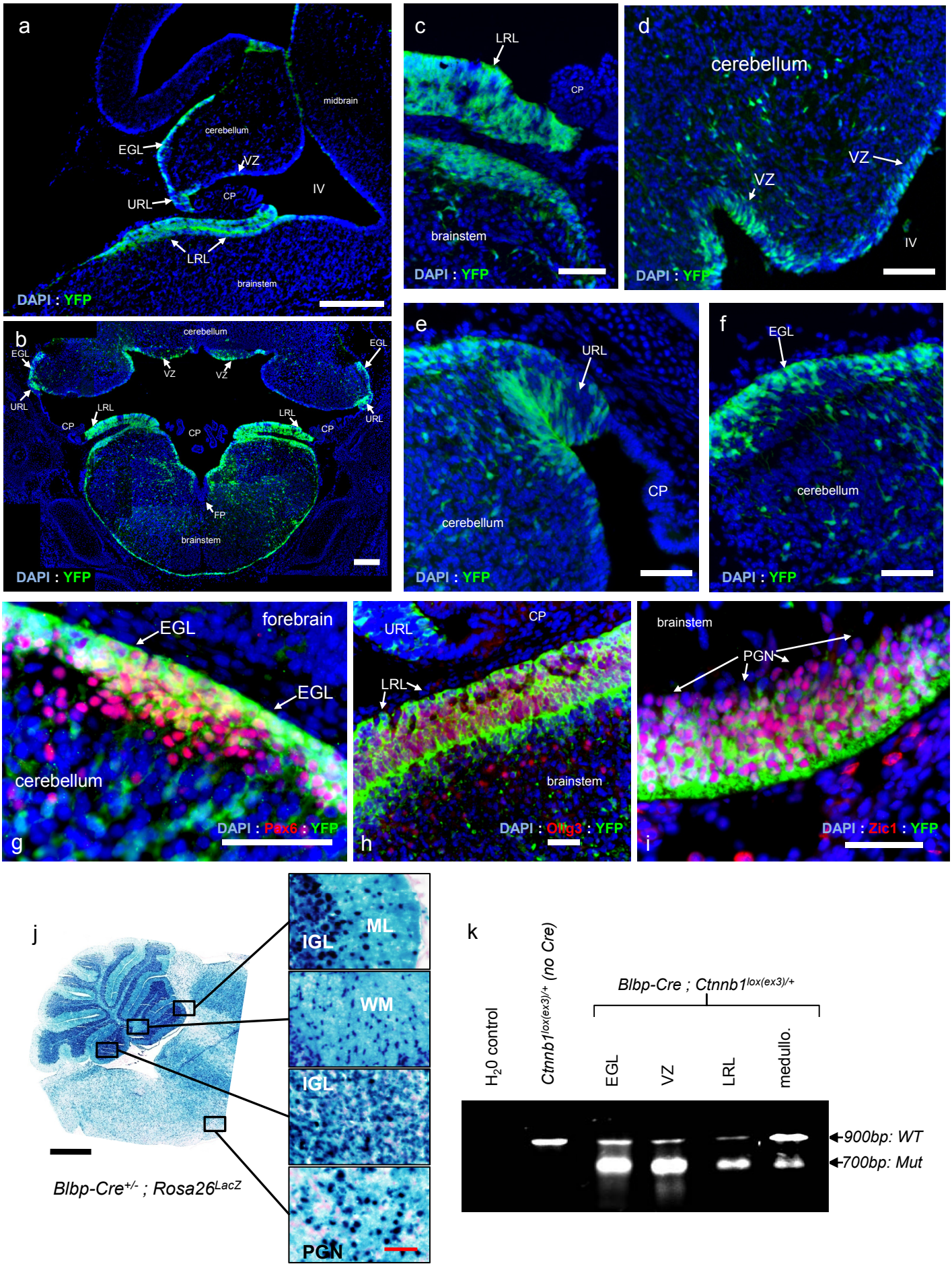
a
midbrain
cerebellum
EGL
VZ
IV
URL
CP
LRL
brainstem
DAPI : YFP
b
cerebellum
EGL
VZ
VZ
EGL
URL
LRL
LRL
URL
CP
CP
CP
FP
brainstem
DAPI : YFP
c
LRL
CP
brainstem
DAPI : YFP
d
cerebellum
VZ
VZ
IV
DAPI : YFP
e
URL
CP
cerebellum
DAPI : YFP
f
EGL
cerebellum
DAPI : YFP
g
EGL
forebrain
EGL
cerebellum
DAPI : Pax6 : YFP
h
URL
CP
LRL
brainstem
DAPI : Olig3 : YFP
i
brainstem
PGN
DAPI : Zic1 : YFP
j
ML
IGL
WM
IGL
PGN
Blbp-Cre+/- ; Rosa26LacZ
k
H20 control
Ctnnb1lox(ex3)/+ (no Cre)
Blbp-Cre ; Ctnnb1lox(ex3)/+
EGL
VZ
LRL
medullo.
900bp: WT
700bp: Mut

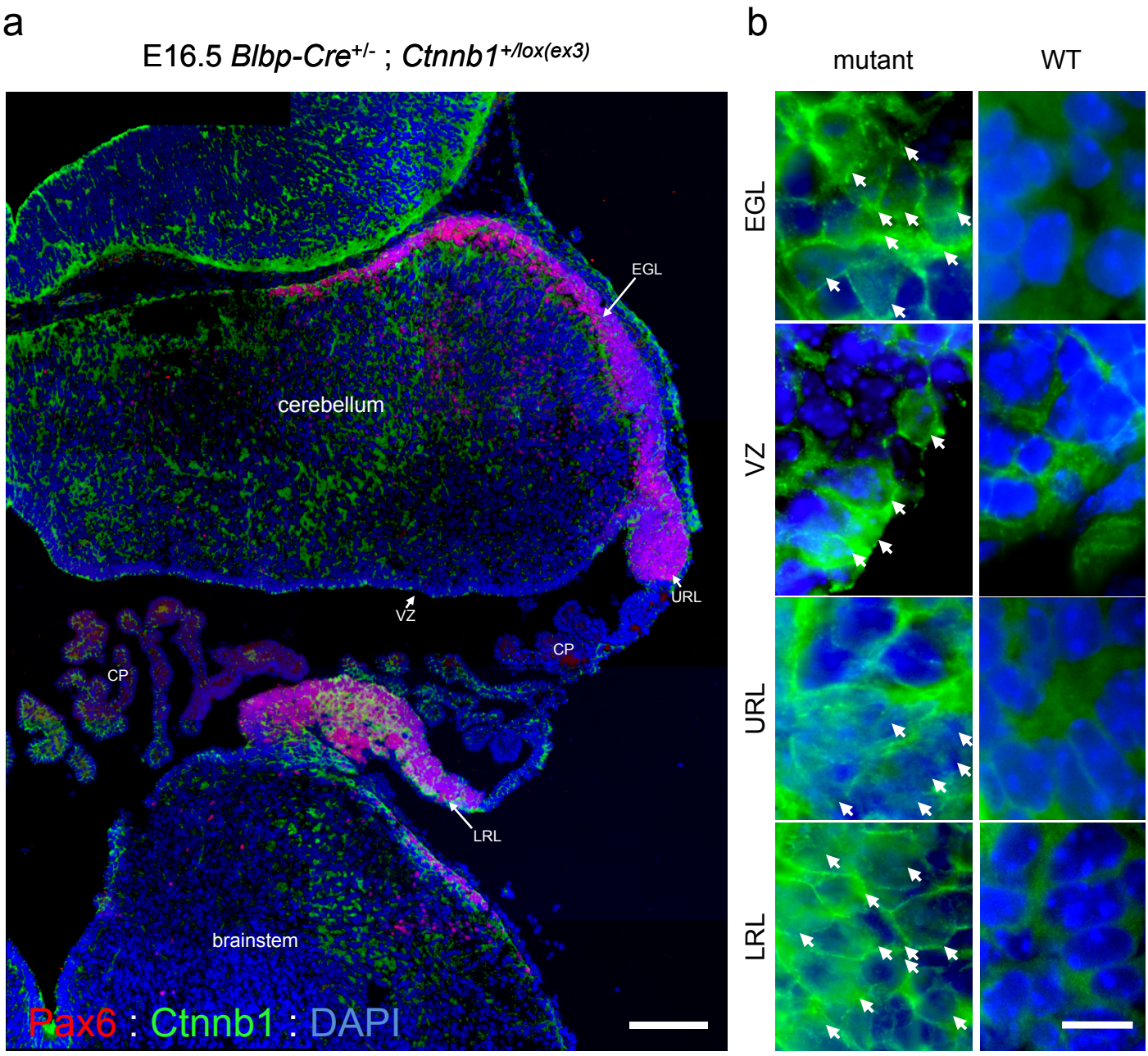

Supplemental Figure 6. *Blbp-Cre* activates aberrant high-level mutant nuclear Ctnnb1 expression throughout germinal zones in the hindbrains of *Blbp-Cre* ; *Ctnnb1*$^{+/lox(ex3)}$ mice. (a) Coronal section through the hindbrain of an embryonic day (E) 16.5 *Blbp-Cre* ; *Ctnnb1*$^{+/lox(ex3)}$ mouse analyzed by Pax6/Ctnnb1 co-immunoflourescence. Scale bar=100µm). **(b)** Left panels show high power views of Ctnnb1 (green) and DAPI (blue) immunofluorescence analysis of the upper rhombic lip (URL)/external germinal layer (EGL); ventricular zone (VZ); and lower rhombic lip (LRL) from the same section of 16.5 *Blbp-Cre* ; *Ctnnb1*$^{+/lox(ex3)}$ mouse hindbrain shown in (a). Comparative sections of wild-type (WT) mice are shown right. Note the markedly increased level of Ctnnb1 expression, especially nuclear expression (arrows), in mutant relative to WT mice. Together with genetic evidence of *Ctnnb1*$^{+/lox(ex3)}$ recombination (Supplemental Figure 5k) these data confirm mutational activation of Ctnnb1 in hindbrain germinal zones. (Scale bar=15µm). CP=choroid plexus.

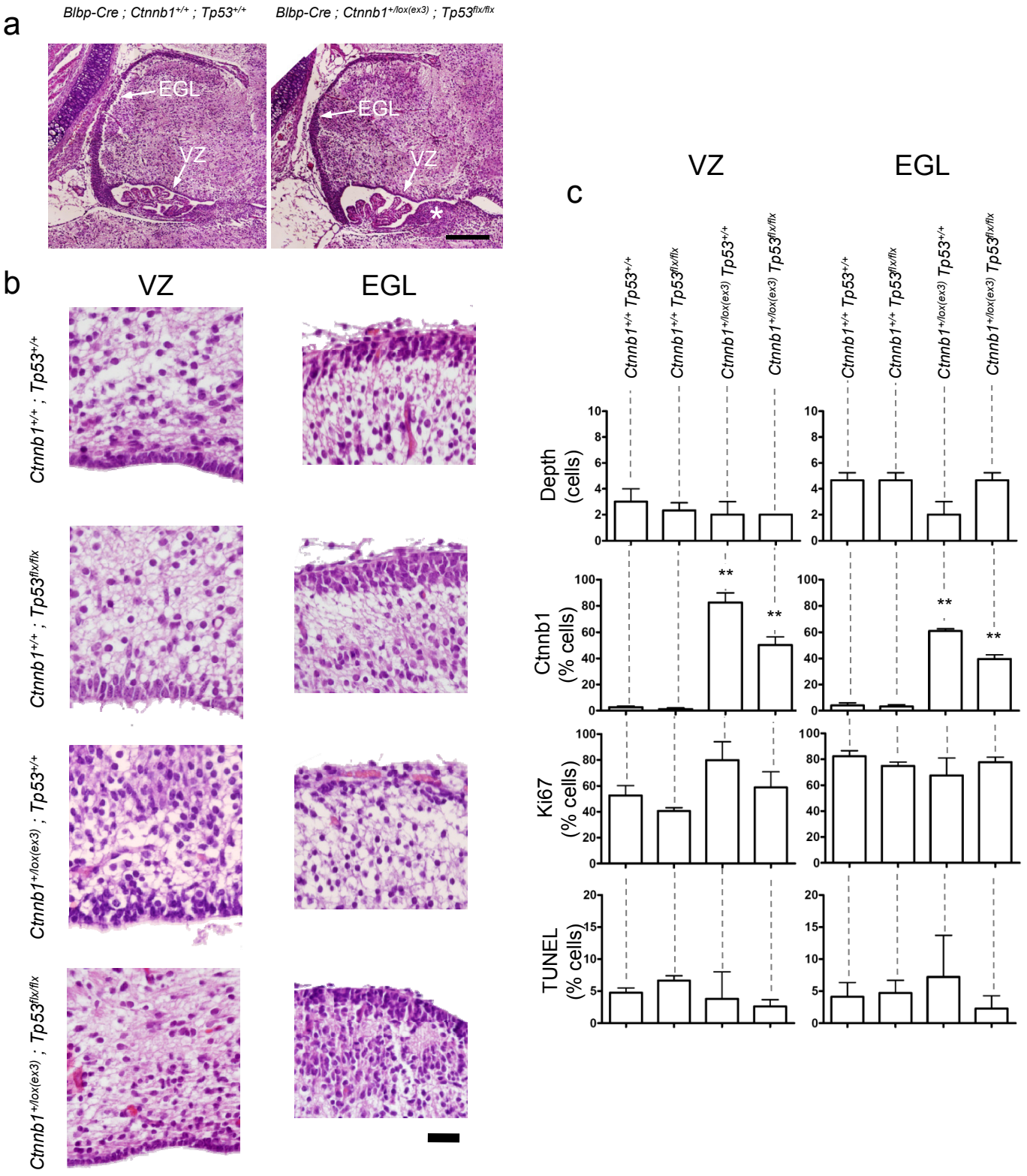

Supplemental Figure 7. Mutant-*Ctnnb1* has little impact on the ventricular zone (VZ) or external germinal layer (EGL) of the developing cerebellum. (a) Sagittal hematoxylin and eosin (H&E) stained sections of the hindbrain of embryonic day (E) E16.5 mice of the indicated genotype showing the VZ and EGL. Arrows indicate the common region of the EGL and VZ shown at high power in each mouse in (b). Note the aberrantly expanded lower rhombic lip in the *Ctnnb1* mutant mouse (*). Scale bar=100 µm. **(b)** High power views of the VZ (left) and EGL (right) of mice of the indicated genotype. Note all mice carried the *Blbp-Cre* transgene. Common scale bar=50 µm. **(c)** Graphs report the average depth of, and percentage of Ctnnb1 nuclear immunoreactive, TUNEL and Ki67 positive cells in, the VZ or EGL of the indicated mice. n≥3 mice per group, Error bars=S.D., exact Mann -Whitney P values , **≤0.005.

Supplemental Figure 8. Mutant-*Ctnnb1* has little impact on the proliferation, migration and differentiation of granule neuron precursor cells (GNPCs) in the external germinal layer (EGL) of the developing cerebellum. (a) Sagittal view of the hindbrain of an E14.5 *Atoh1-Cre* (Matei et al., Dev Dyn, 2005) ; *RosaYFP* mouse demonstrating efficient recombination in GNPCs of the EGL. Scale bar=120µm. **(b)** High power view of YFP/Pax6 co-immunofluorescence of the EGL, molecular layer (ML) and internal granule layer (IGL) of the same mouse shown in (a) demonstrating *Atoh1-Cre* mediated recombination in $Pax6^+$ GNPCs. Scale bar=50µm. **NB.** The 'JQ2 1.7Kb-*Atoh1* enhancer element' from Jane Johnson was used by Matei et al., to generate in the *Atoh1-Cre* transgene. This same *Atoh1-Cre* has been shown to drive extensive hyperplasia of the EGL and SHH-subtype medulloblastoma in conditional *Ptch1* deleted mice (see Ref. 7 main manuscript). **(c)** YFP/Olig3 co-immunofluorescence of an E14.5 *Atoh1-Cre* ; *RosaYFP* mouse. Although the endogenous *Atoh1* allele is expressed in cells of the lower rhombic lip (LRL, Machold and Fischell, Neuron, 2005; Landsberg et al., Neuron 2005) the 'JQ2 1.7Kb-*Atoh1* enhancer element' in the *Atoh1-Cre* transgene does not drive efficient recombination in $Olig3^+$ progenitors of the LRL. Scale bar=200µm **(d)** In keeping with the lack of *Atoh1-Cre* mediated recombination in the LRL, no $Zic1^+$ mossy fiber neurons of the pontine grey nucleus (PGN) were YFP^+. Scale bar=100µm. Inset shows high power view of $YFP^-/Zic1^+$ PGN mossy fiber neurons. **(e)** Rare scattered populations of $YFP^+/Zic1^+$ cells were seen in the brainstem of *Atoh1-Cre* ; *RosaYFP* mice demonstrating some recombination was targeted in rare LRL progenitors. **NB. The lack of recombination in LRL progenitors in *Atoh1-Cre* ; *RosaYFP* mice is in stark contrast to the extensive recombination seen in these cells in *Blbp-Cre* ; *RosaYFP* mice (compare a-e here with Supplemental Figure 5)**. The same *Atoh1-Cre* mouse employed in (a-e) was crossed with $Ctnnb1^{+/lox(ex3)}$ mice to activate mutant Ctnnb1 expression in GNPCs. **(f)** Hematoxylin and eosin stained coronal, **(g)** Zic1 immunofluorescence stained coronal, **(h)** Zic1 immunofluorescence stained sagittal, and **(i)** Ki67 immunofluorescence stained sagittal sections of early postnatal day (P) *Atoh1-Cre* ; $Ctnnb1^{+/lox(ex3)}$ hindbrains. Detailed histologic review of these mice revealed grossly normal hindbrains with no evidence of the aberrant LRL development seen in *Blbp-Cre* ; $Ctnnb1^{+/lox(ex3)}$ mice (**compare with Figure 2 in the main manuscript.** Scale bar=200µm). **(j)** High power view of the EGL of a P7 *Atoh1-Cre* ; $Ctnnb1^{+/lox(ex3)}$ mouse confirming nuclear expression of Ctnnb1 (**Compare with Supplemental Figure 6b). (k)** As a second, independent way of demonstrating GNPCs are resistant to mutant-*Ctnnb1*, we generated a transgenic mouse in which a constitutively active $Ctnnb1^{\Delta N90}$-Enhanced Green Fluorescence Protein (EGFP) fusion protein was driven by the same 'JQ2 1.7Kb-*Atoh1* enhancer element' (generous gift of Jane Johnson) used to drive Cre expression in *Atoh1-Cre* mice shown in (a-j). *Atoh1-*$Ctnnb1^{\Delta N90GFP}$ mice express high levels of the $Ctnnb1^{\Delta N90GFP}$ fusion protein in the EGL at E14.5 **(l)** and P5 **(m)**. Scale bar=120µm. GFP/Ctnnb1 co-immunoflourescence of these same mice confirmed nuclear (activated) expression of the mutant Ctnnb1-GFP fusion protein in P7 GNPCs (arrows). Scale bar=50µm. **(o)** In keeping with our analysis of *Atoh1-Cre* ; *RosaYFP* and *Atoh1-Cre* ; $Ctnnb1^{+/lox(ex3)}$ these mice did not express $Ctnnb1^{\Delta N90GFP}$ in the LRL and developed with grossly normal hindbrains (including normal LRL development). Scale bar=800 µm. **(p)** Finally, we tested if isolated cultures of GNPCs might respond to aberrant WNT signals. We FACS sorted GNPCs from *Atoh1-Gfp* cerebella and challenged these *ex vivo* with mutant *Ctnnb1* or Wnt1 ligand. Graphs report the average proliferation (3H-thymidine incorporation, n=4 replicates per group) of Gfp^+ GNPCs transduced with control ($MSCV^{CTRL}$) or mutant-Ctnnb1 ($MSCV^{Ctnnb1}$) retrovirus and/or exposed to the mitogens Shh or Wnt1. Error bars are S.E., (Exact Mann Whitney P values , ***, <0.005, ***<0.0005 are relative to the appropriate control).

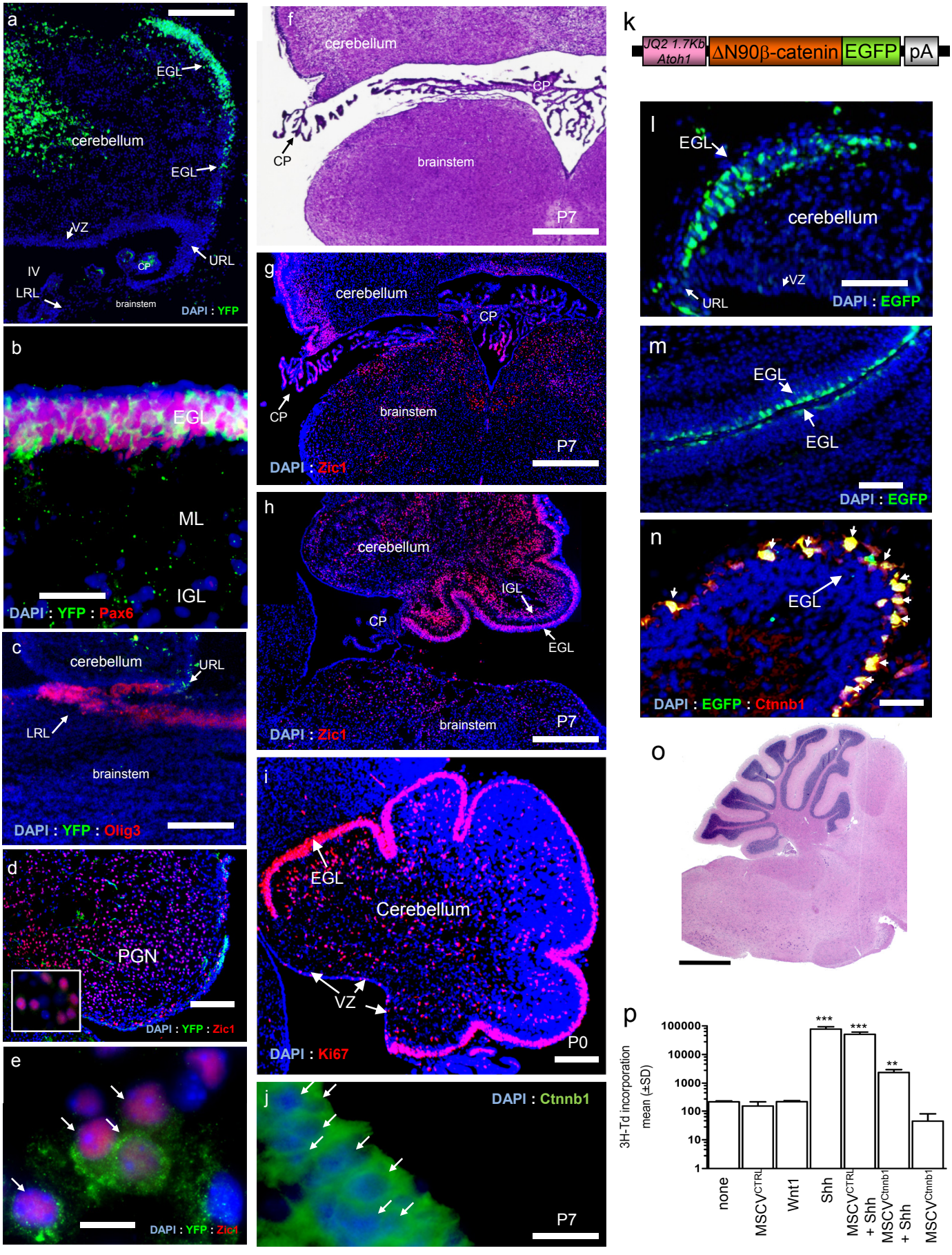
Atoh1-Cre ; RosaYFP
Atoh1-Cre ; Ctnnb1+/lox(ex3)
Atoh1- Ctnnb1ΔN90GF
a
EGL
cerebellum
EGL
VZ
URL
IV
CP
LRL
brainstem
DAPI : YFP
b
EGL
ML
IGL
DAPI : YFP : Pax6
c
cerebellum
URL
LRL
brainstem
DAPI : YFP : Olig3
d
PGN
DAPI : YFP : Zic1
e
DAPI : YFP : Zic1
f
cerebellum
CP
CP
brainstem
P7
g
cerebellum
CP
CP
brainstem
DAPI : Zic1
P7
h
cerebellum
IGL
CP
EGL
DAPI : Zic1
brainstem
P7
i
EGL
Cerebellum
VZ
DAPI : Ki67
P0
j
DAPI : Ctnnb1
P7
k
UQ2 1.7Kb Atoh1
ΔN90β-catenin
EGFP
pA
l
EGL
cerebellum
VZ
URL
DAPI : EGFP
m
EGL
EGL
DAPI : EGFP
n
EGL
DAPI : EGFP : Ctnnb1
o
p
3H-Td incorporation mean (±SD)
100000
10000
1000
100
10
1
***
***
**
none
MSCVCTRL
Wnt1
Shh
MSCVCTRL + Shh
MSCVCtnnb1 + Shh
MSCVCtnnb1

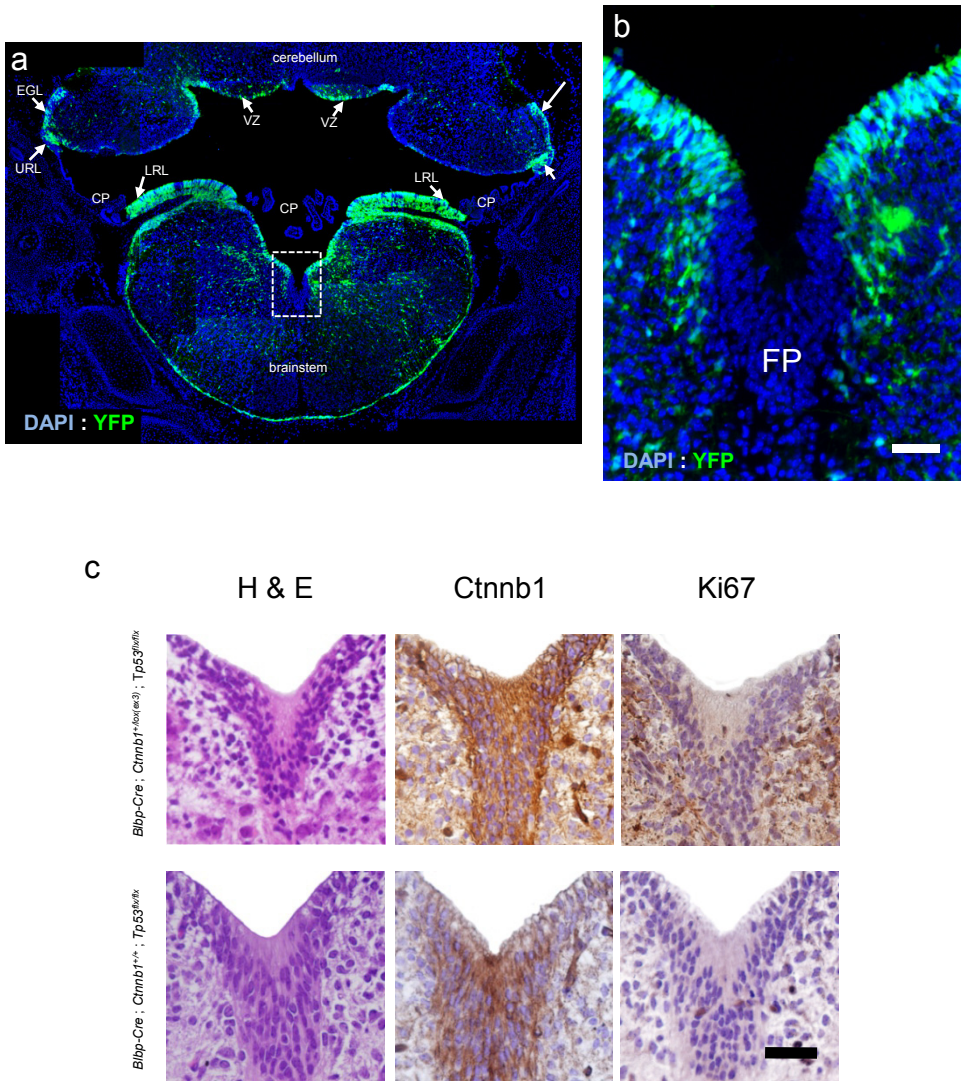

Supplemental Figure 9. *Blbp-Cre*-dependent mutation of *Ctnnb1*$^{flox(ex3)}$ does not target the floor plate (FP). (a) Reproduction of Supplemental Figure 5b showing a coronal view of an embryonic day (E) 14.5 *Blbp-Cre* ; *RosaYFP* mouse demonstrating efficient Cre-induced recombination in germinal zones of the developing hindbrain. A high power view of the boxed area is shown in **(b)** illustrating that the *Blbp-Cre* allele does not induce recombination in FP cells. Scale bar is 50µm. **(c)** High power views of the FP stained with hematoxylin and eosin (H & E) or immunostained for Ctnnb1 and Ki67. Note normal morphology and lack of nuclear Ctnnb1 regardless of *Ctnnb1*$^{+/flox(ex3)}$ status. Scale bar is 50µm.

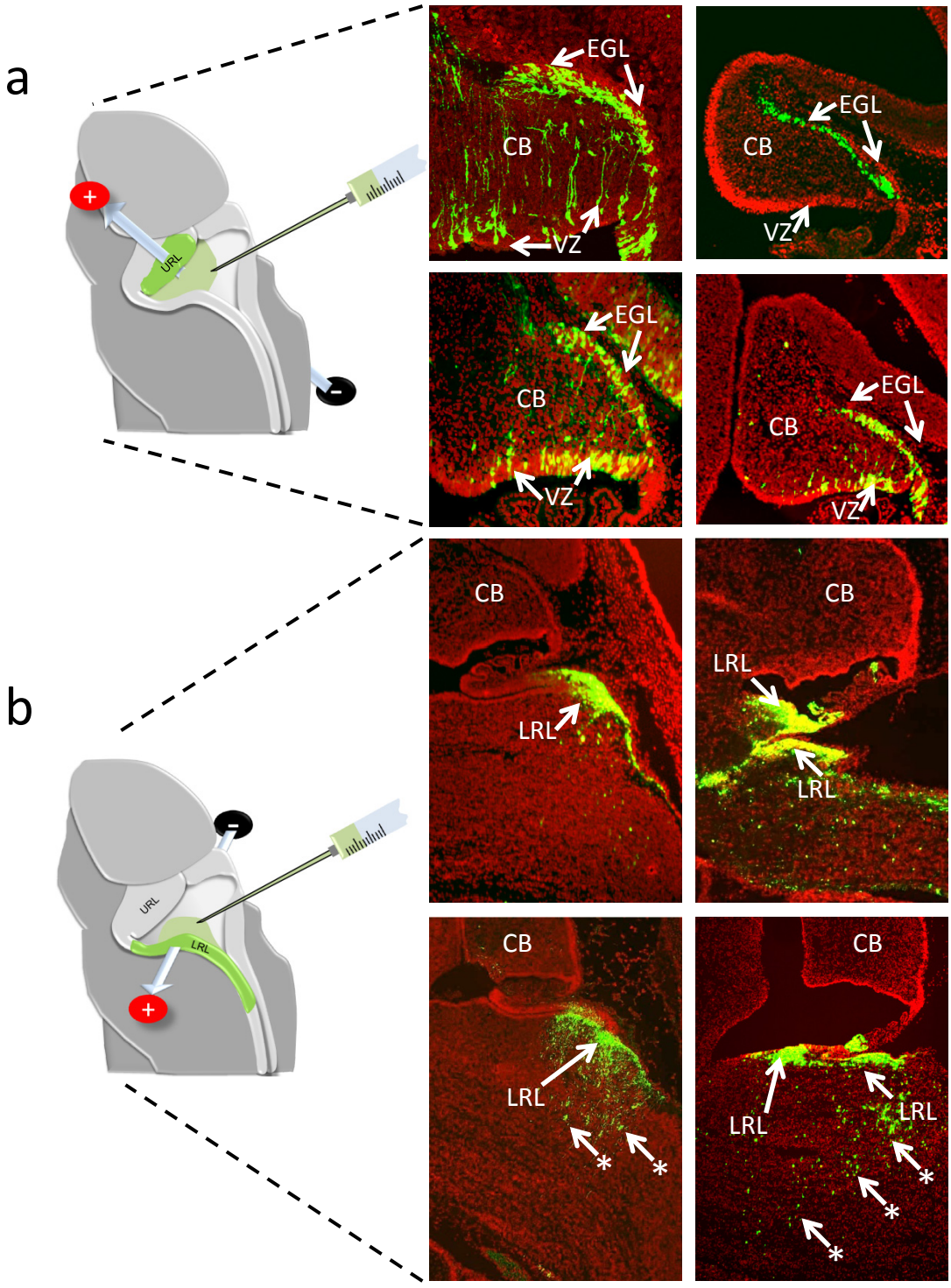

Supplemental Figure 10. Directed electroporation of a plasmid encoding green fluorescence protein (GFP) labels distinct compartments of the E12.5 hindbrain. (a) Cartoon to the left shows the direction of electroporation used to label the upper rhombic lip (URL) at E12.5. Panels to the right show sagittal sections of the hindbrains of four separate E16.5 mice in which the URL was labeled at E12.5. GFP^+ cells are found throughout the external germinal layer (EGL) and the ventricular zone (VZ) of the cerebellum (CB). **(b)** Cartoon to the left shows the direction of electroporation used to label the lower rhombic lip (LRL) including r6-r8. Panels to the right show sagittal sections of the hindbrains of four separate E16.5 in which the LRL was labeled at E12.5. Note cells within the EGL or SVZ are not labeled with this approach. (*) indicates cells seen migrating away from the LRL (see also Supplemental Figure 10).

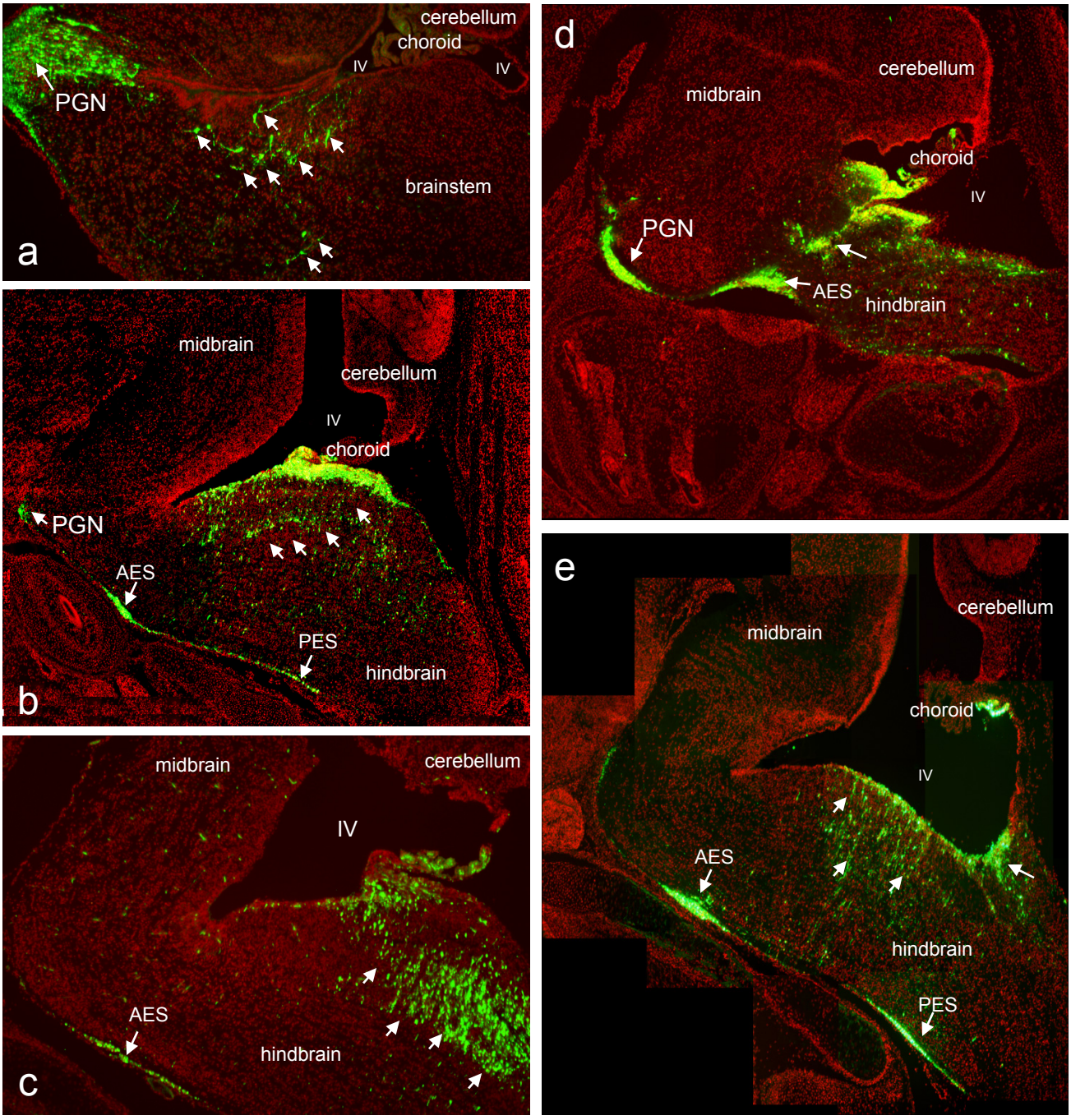

Supplemental Figure 11. Lower rhombic lip (LRL) cells electroporated at E12.5 with green fluorescence protein (GFP) migrate to form nuclei throughout developing hindbrain. (a-c) Three different sagittal sections through the brain of a single embryonic day (E) 16.5 mouse in which the LRL was electroporated with GFP at E12.5 as described in Supplemental Figure 9b. Note the dispersal of GFP^+ cells throughout the hindbrain including the pontine grey nucleus (PGN) as well as multiple sites covering the dorso-ventral and rostro-caudal hindbrain axis. GFP^+ cells in sites compatible with the mossy fibre anterior extramural stream (AES) and posterior extramural stream (PES) are indicated. Additional arrows indicate intramural migrating GFP^+ cells. Note the cerebellum and midbrain are unlabelled indicating the accuracy of LRL electroporation. **(d)** and **(e)** show sagittal brain sections of two additional E16.6 mice in which the LRL was also electroporated with GFP at E12.5. Again note the wide dispersal of GFP^+ cells throughout the hindbrain and mossy fibre migratory streams with sparing of the cerebellum and midbrain.

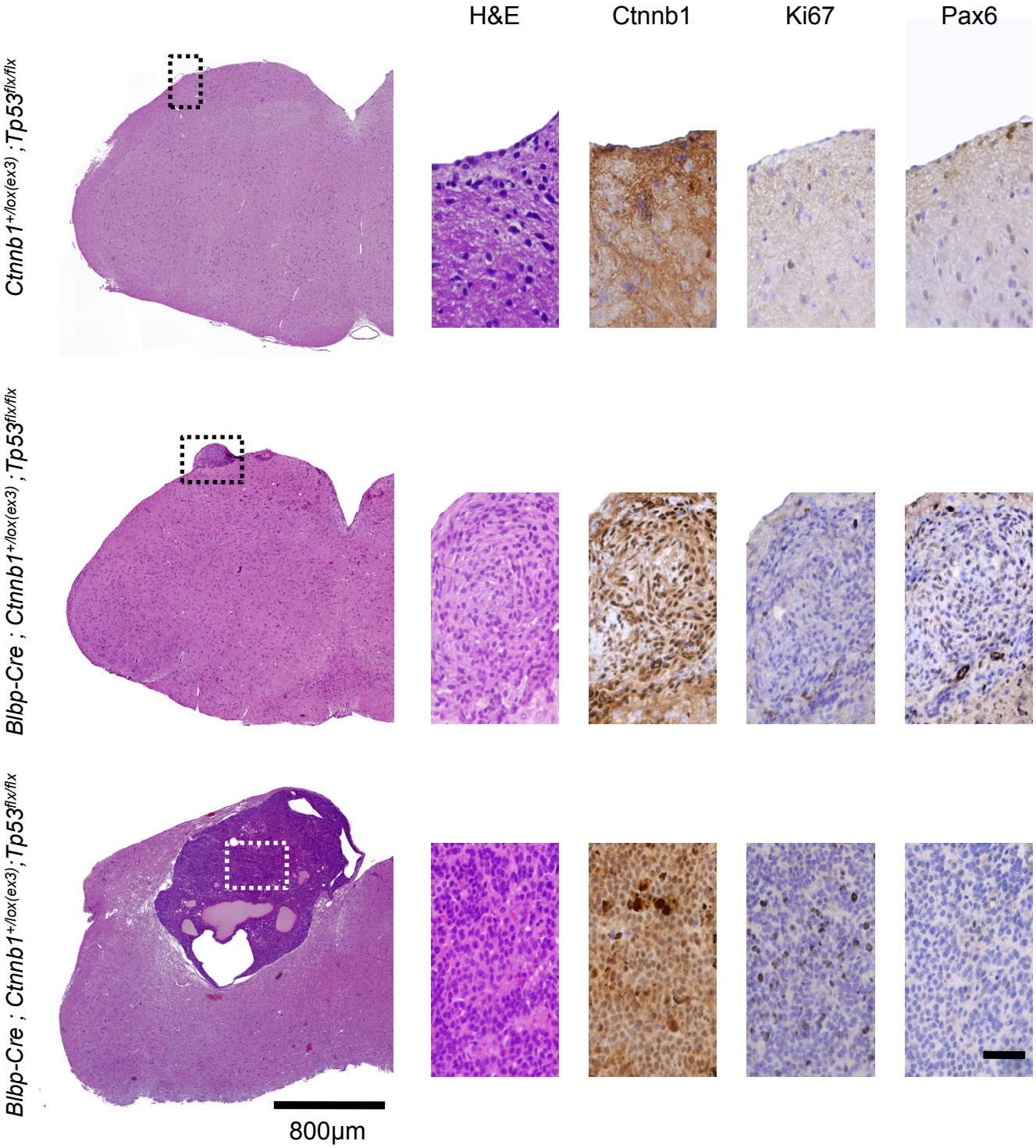

Supplemental Figure 12. Early tumors in *Blbp-Cre ; Ctnnb1*$^{+/flox(ex3)}$ *; Tp53*$^{flx/flx}$ adult mice are restricted to the floor of the IV ventricle in the region occupied in embryos by the lower rhombic lip. Left, low power coronal sections of the brainstem of 6 month old adult mice of the indicated genotype. Right, high power views of sections within the boxed regions shown left that have been stained with hematoxylin and eosin or the indicated immunostain. Scale bar for high power views is 50µm. Note the early lesions in *Blbp-Cre ; Ctnnb1*$^{+/flox(ex3)}$ *; Tp53*$^{flx/flx}$ mice are confined to the brainstem (boxed by dotted line). The cerebellum was unaffected in these animals. Nuclear Ctnnb1 and Ki67 immunostaining was seen only in the lesions of *Blbp-Cre ; Ctnnb1*$^{+/flox(ex3)}$ *; Tp53*$^{flx/flx}$ mice.

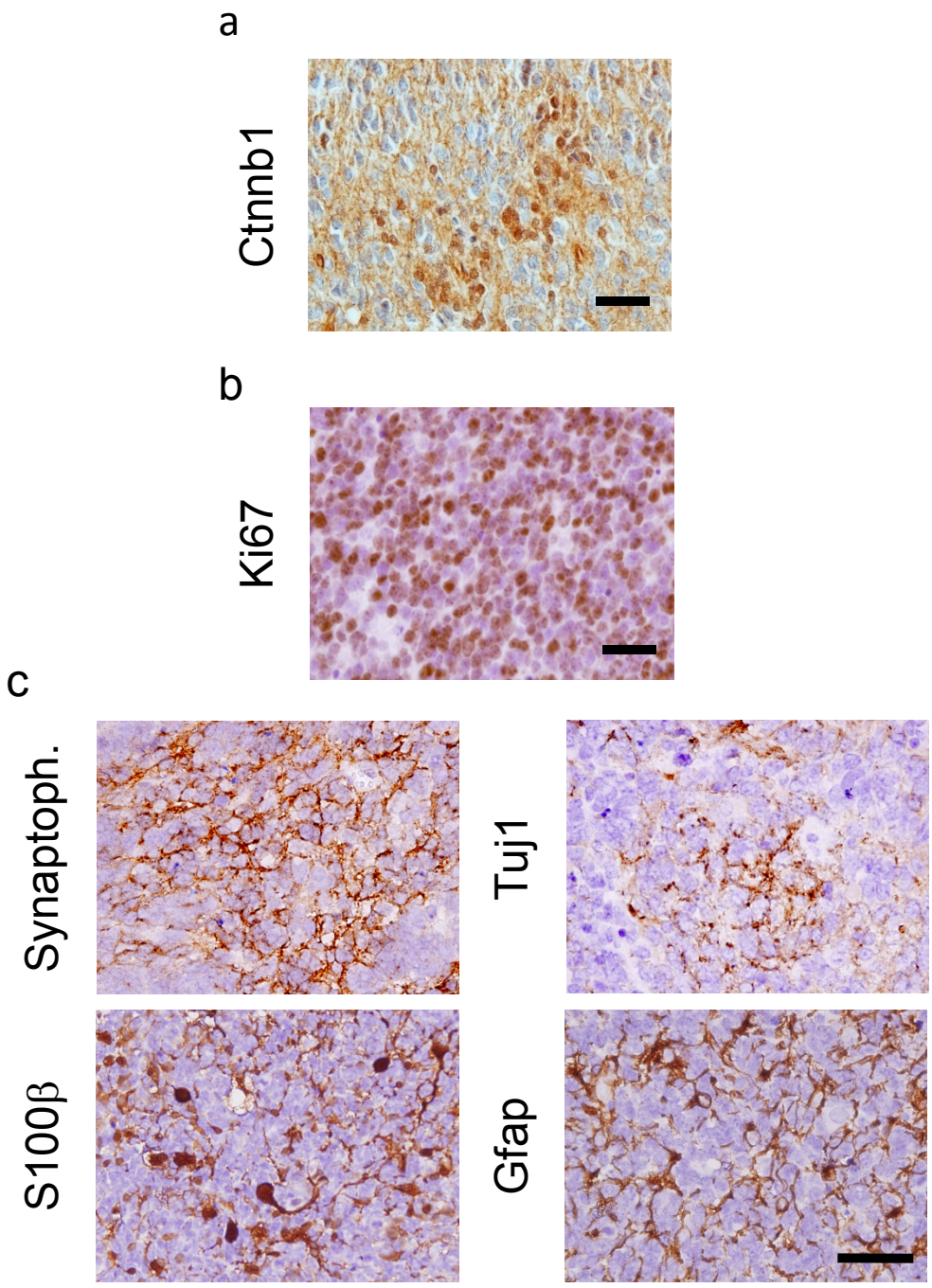

Supplemental Figure 13. Medulloblastomas arising in *Blbp-Cre ; Ctnnb1*$^{+/flox(ex3)}$ *; Tp53*$^{flx/flx}$ mice display an immunoprofile similar to that of human WNT-subtype medulloblastoma. (a) CTNNB1 immunohistochemical staining of a section of human WNT-subtype medulloblastoma. Note the CTNNB1 nuclear staining in many but not all tumor cells. Compare with Figure 3d(iv) in the main paper. **(b)** Ki67 immunohistochemical staining of a section of *Blbp-Cre*$^{+/-}$; *Ctnnb1*$^{+/lox(ex3)}$; *Tp53*$^{flx/flx}$ mouse medulloblastoma. Note the frequent Ki67 nuclear staining typical of human medulloblastoma. **(c)** Panels show photomicroraphs of medulloblastomas arising in *Blbp-Cre ; Ctnnb1*$^{+/flox(ex3)}$ *; Tp53*$^{flx/flx}$ mice that have been immunostained for neuronal (Tuj1 and Synaptophysin) and glial (S100β and Gfap) markers. Scale bar is 50μm.

Tumor:	Medulloblastoma	Medulloblastoma
Histology	Classic	Classic
Metastasis:	M0	M0
Sex:	Male	Male
Age (ys):	10	12.7
CTNNB1 mut:	S37F	S33C
Tumor *Tp53*:	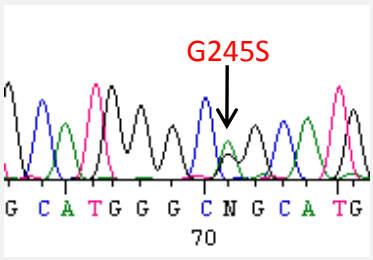	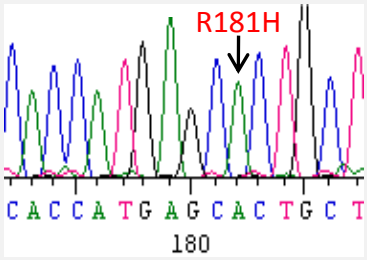

Supplemental Figure 14. Concurrent somatic *CTNNB1* and *TP53* mutations in two sporadic human medulloblastomas.

Supplemental Table 1: Expression distribution of signature genes of human SHH-subtype and WNT-subtype medulloblastoma in the E15.5 mouse EGL, VZ, and LRL.

Gene	Signature	EGL	VZ	LRL	Sup. Dataset 1	Gene	Signature	EGL	VZ	LRL	Sup. Dataset 1
Gas1	SHH	Y	Y	Y	Y	Myo1b	WNT	Y	Y	Y	N
Rcn3	SHH	Y	Y	Y	N	Hspa5	WNT	Y	Y	Y	N
Plxnb2	SHH	Y	Y	Y	N	Fzd10	WNT	Y	Y	Y	Y
Flna	SHH	Y	Y	Y	N	Calu	WNT	Y	Y	Y	N
Ephb4	SHH	Y	Y	Y	N	Armet	WNT	Y	Y	Y	N
Lamc1	SHH	Y	Y	Y	N	Ctsk	WNT	Y	Y	Y	N
Sf3a2	SHH	Y	Y	Y	N	Ror2	WNT	Y	Y	Y	N
Trim28	SHH	Y	Y	Y	Y	Lef1	WNT	Y	Y	Y	Y
Nap1l1	SHH	Y	Y	Y	N	Rgl1	WNT	Y	Y	Y	N
Igfbp5	SHH	Y	Y	Y	Y	Pmp22	WNT	Y	Y	Y	N
Sema6a	SHH	Y	Y	Y	Y	Pax3	WNT	Y	Y	Y	Y
Cxcr4	SHH	Y	Y	Y	Y	Tnc	WNT	N	Y	Y	Y
Eef1d	SHH	Y	Y	Y	N	Gad1	WNT	N	Y	Y	Y
Itga7	SHH	Y	Y	Y	N	Cdkn1c	WNT	N	Y	Y	N
Csnk1e	SHH	Y	Y	Y	Y	Lrrn3	WNT	N	Y	Y	Y
Mycl1	SHH	Y	Y	Y	Y	Odz3	WNT	N	Y	Y	Y
Unc5c	SHH	Y	Y	Y	Y	Dpf3	WNT	N	Y	Y	N
Notch2	SHH	Y	Y	Y	Y	Plcb1	WNT	N	Y	Y	N
Ilf3	SHH	Y	Y	Y	N	Epha4	WNT	N	Y	Y	Y
ProSAPip1	SHH	Y	Y	Y	N	Slc13a3	WNT	N	Y	Y	N
Nhlh1	SHH	Y	Y	Y	Y	Pkp4	WNT	Y	N	Y	N
Lmo4	SHH	Y	Y	Y	Y	Wif1	WNT	Y	N	Y	N
Plk3	SHH	Y	Y	Y	N	Ddr2	WNT	Y	N	Y	N
Pygb	SHH	Y	Y	Y	N	Lmo2	WNT	Y	N	Y	Y
Pbx3	SHH	N	Y	Y	Y	Col9a3	WNT	Y	N	Y	Y
Pscd2	SHH	N	Y	Y	N	Epha3	WNT	N	N	Y	Y
Sox9	SHH	N	Y	Y	N	Lgl2	WNT	N	N	Y	N
Rgs16	SHH	N	Y	Y	N	Map2k6	WNT	N	N	Y	N
Atoh1	SHH	Y	N	Y	Y	Nefl	WNT	N	N	Y	N
Rpl10	SHH	Y	N	Y	N	Th	WNT	N	N	Y	Y
Atic	SHH	Y	N	Y	N	Col5a1	WNT	N	N	Y	Y
Slc29a1	SHH	Y	N	Y	N	Twist1	WNT	N	N	Y	Y
Sfrp1	SHH	Y	N	Y	Y	Chn1	WNT	N	N	Y	N
Rgs9	SHH	N	N	Y	N	Atbf1	WNT	N	N	Y	Y
Lamc3	SHH	Y	Y	N	N	Isl1	WNT	N	N	Y	Y
Col4a5	SHH	Y	Y	N	Y	Lbh	WNT	N	N	Y	N
Sh3bgrl3	SHH	Y	Y	N	N	Arhgap4	WNT	Y	Y	N	N
Sostdc1	SHH	N	Y	N	Y	Ppfibp2	WNT	Y	N	N	N
Apod	SHH	Y	N	N	Y	Adam12	WNT	Y	N	N	N
Mc5r	SHH	Y	N	N	N	Bmp4	WNT	N	N	N	Y
Wasf2	SHH	Y	N	N	N	Fzd6	WNT	N	N	N	Y
Ntrk3	SHH	Y	N	N	N	Galr1	WNT	N	N	N	Y

Gene	Signature	EGL	VZ	LRL	Sup. Dataset 1
Krt17	SHH	Y	N	N	N
Timp3	SHH	Y	N	N	N
Cybrd1	SHH	Y	N	N	N
Ngfr	SHH	Y	N	N	Y
Dcn	SHH	N	N	N	Y
Cxcl12	SHH	N	N	N	Y
Igf2	SHH	N	N	N	Y
Edg4	SHH	N	N	N	N
Galtn2	SHH	N	N	N	N
Gnas	SHH	N	N	N	N
Fbln5	SHH	N	N	N	N
Ptx3	SHH	N	N	N	N
Arhgef7	SHH	N	N	N	N
Rnf130	SHH	N	N	N	N
F2r	SHH	N	N	N	N
Col6a1	SHH	N	N	N	Y
Ndrg1	SHH	N	N	N	N
Dpf3	SHH	N	N	N	N
Nmu	SHH	N	N	N	N
Chrna7	SHH	N	N	N	Y
Satb2	SHH	N	N	N	Y
Sez6l	SHH	N	N	N	N
TOTAL		40	32	34	
%		63	50	53	

Gene	Signature	EGL	VZ	LRL	Sup. Dataset 1
Foxa1	WNT	N	N	N	Y
Lhx6	WNT	N	N	N	Y
Tph1	WNT	N	N	N	Y
Adam11	WNT	N	N	N	N
TOTAL		20	21	36	
%		43	46	78	

Chi square **<0.05**